

Self-calibration of BICEP1 three-year data and constraints on astrophysical polarization rotation

J. P. Kaufman,^{1,*} N. J. Miller,² M. Shimon,^{3,1} D. Barkats,⁴ C. Bischoff,⁵ I. Buder,⁵ B. G. Keating,¹ J. M. Kovac,⁵ P. A. R. Ade,⁶ R. Aikin,⁷ J. O. Battle,⁸ E. M. Bierman,¹ J. J. Bock,^{7,8} H. C. Chiang,⁹ C. D. Dowell,⁸ L. Duband,¹⁰ J. Filippini,⁷ E. F. Hivon,¹¹ W. L. Holzapfel,¹² V. V. Hristov,⁷ W. C. Jones,¹³ S. S. Kernasovskiy,^{14,15} C. L. Kuo,^{14,15} E. M. Leitch,¹⁶ P. V. Mason,⁷ T. Matsumura,¹⁷ H. T. Nguyen,⁸ N. Ponthieu,¹⁸ C. Pryke,¹⁹ S. Richter,⁷ G. Rocha,^{7,8} C. Sheehy,¹⁶ M. Su,^{20,21} Y. D. Takahashi,¹² J. E. Tolan,^{14,15} and K. W. Yoon^{14,15}

¹*Department of Physics, University of California, San Diego, 9500 Gilman Drive, La Jolla, California 92093-0424, USA*

²*Observational Cosmology Laboratory, Code 665, Goddard Space Flight Center, 8800 Greenbelt Road, Greenbelt, Maryland 20771, USA*

³*School of Physics and Astronomy, Tel Aviv University, Tel Aviv 69978, Israel*

⁴*Joint ALMA Observatory, ESO, Santiago 19001, Chile*

⁵*Harvard-Smithsonian Center for Astrophysics, 60 Garden Street MS 42, Cambridge, Massachusetts 02138, USA*

⁶*Department of Physics and Astronomy, University of Wales, Cardiff, CF24 3YB Wales, United Kingdom*

⁷*Department of Physics, California Institute of Technology, Pasadena, California 91125, USA*

⁸*Jet Propulsion Laboratory, Pasadena, California 91109, USA*

⁹*Astrophysics and Cosmology Research Unit, University of KwaZuluNatal, Durban 4041, South Africa*

¹⁰*SBT, Commissariat à l'Energie Atomique, Grenoble 38054, France*

¹¹*Institut d'Astrophysique de Paris, Paris 75014, France*

¹²*Department of Physics, University of California at Berkeley, Berkeley, California 94720, USA*

¹³*Department of Physics, Princeton University, Princeton, New Jersey 08544, USA*

¹⁴*Stanford University, Palo Alto, California 94305, USA*

¹⁵*Kavli Institute for Particle Astrophysics and Cosmology (KIPAC), Sand Hill Road 2575, Menlo Park, California 94025, USA*

¹⁶*University of Chicago, Chicago, Illinois 60637, USA*

¹⁷*High Energy Accelerator Research Organization (KEK), Ibaraki 305-0801, Japan*

¹⁸*Institut d'Astrophysique Spatiale, Université Paris-Sud, Orsay 91405, France*

¹⁹*Department of Physics, University of Minnesota, Minneapolis, Minnesota 55455, USA*

²⁰*Department of Physics, Massachusetts Institute of Technology, 77 Massachusetts Avenue, Cambridge, Massachusetts 02139, USA*

²¹*MIT-Kavli Center for Astrophysics and Space Research, 77 Massachusetts Avenue, Cambridge, Massachusetts 02139, USA*

(Received 22 January 2014; published 24 March 2014)

Cosmic microwave background (CMB) polarimeters aspire to measure the faint B -mode signature predicted to arise from inflationary gravitational waves. They also have the potential to constrain cosmic birefringence, rotation of the polarization of the CMB arising from parity-violating physics, which would produce nonzero expectation values for the CMB's temperature to B -mode correlation (TB) and E -mode to B -mode correlation (EB) spectra. However, instrumental systematic effects can also cause these TB and EB correlations to be nonzero. In particular, an overall miscalibration of the polarization orientation of the detectors produces TB and EB spectra which are degenerate with isotropic cosmological birefringence, while also introducing a small but predictable bias on the BB spectrum. We find that BICEP1 three-year spectra, which use our standard calibration of detector polarization angles from a dielectric sheet, are consistent with a polarization rotation of $\alpha = -2.77^\circ \pm 0.86^\circ(\text{statistical}) \pm 1.3^\circ(\text{systematic})$. We have revised the estimate of systematic error on the polarization rotation angle from the two-year analysis by comparing multiple calibration methods. We also account for the (negligible) impact of measured beam systematic effects. We investigate the polarization rotation for the BICEP1 100 GHz and 150 GHz bands separately to investigate theoretical models that produce frequency-dependent cosmic birefringence. We find no evidence in the data supporting either of these models or Faraday rotation of the CMB polarization by the Milky Way galaxy's magnetic field. If we assume that there is no cosmic birefringence, we can use

*jkaufman@physics.ucsd.edu

the TB and EB spectra to calibrate detector polarization orientations, thus reducing bias of the cosmological B -mode spectrum from leaked E -modes due to possible polarization orientation miscalibration. After applying this “self-calibration” process, we find that the upper limit on the tensor-to-scalar ratio decreases slightly, from $r < 0.70$ to $r < 0.65$ at 95% confidence.

DOI: [10.1103/PhysRevD.89.062006](https://doi.org/10.1103/PhysRevD.89.062006)

PACS numbers: 98.70.Vc

I. INTRODUCTION

The cosmic microwave background (CMB) is a powerful cosmological probe; recombination physics, structure formation, and the cosmological reionization history represent only a small subset of the phenomena probed by its temperature and polarization anisotropy. In addition, several aspects of fundamental physics can be constrained by CMB observations, the most familiar of which are inflationary physics revealed via the imprint of primordial gravitational waves in the polarization of the CMB and the masses of neutrinos which can be probed via gravitational lensing by dark matter. These phenomena create B -mode polarization at the sub- μK level.

Cosmological information can be extracted from the CMB’s power spectra. Out of the six possible pairings of the temperature anisotropy T and polarization E - and B -modes, only four have nonvanishing expectation values in the standard (Λ CDM) cosmological paradigm. The expectation values of the TB and EB cross correlations vanish in the standard cosmological model due to parity symmetry but may assume nonvanishing values in the presence of systematics, astrophysical foregrounds, or, more interestingly, parity-violating departures from the standard models of electromagnetism and gravity. Any mechanism capable of converting E - to B -mode polarization necessarily leaks the temperature to E -mode correlations (TE) and E -mode auto spectrum (EE) to TB and EB , respectively.

A detection of TB and EB correlations of cosmological origin could undermine the fundamental assumptions of parity symmetry and Lorentz invariance by showing that our Universe possesses a small degree of chirality. This phenomenon can be best revealed by CMB polarization where minuscule effects can accrue to observable levels over the 13.8 Gyrs since CMB photons last scattered from the primordial plasma. This preferred chirality can be induced by the coupling of a pseudoscalar field to either Chern-Simons-type terms in the electromagnetic interaction [1–3]

or the Chern-Pontrayagin term in the case of gravitational interactions [4–6]. This work constrains the parameters in a scale-independent cosmological birefringence model as well as investigating frequency-dependent scale-independent models. Current best constraints (not including this work) on scale-independent cosmological birefringence from CMB experiments are shown in Table I. Though constraints on scale-dependent birefringence models have been reported with WMAP data [7–9], we do not provide such constraints in this work. A 3σ detection of cosmic birefringence was reported from combined WMAP, BOOMERanG, and BICEP1 two-year results (while explicitly excluding QUaD data) in [10]. This work was later updated to include the impact of systematic effects at the levels reported by the three experiments and the significance reduced to 2.2σ [11].

BICEP1 has set the most stringent constraints on the CMB’s B -mode power spectrum [16,17] in the multipole range $30 < \ell < 300$. BICEP1 also measured the TB and EB power spectra in this range [16,17]. These TB and EB modes are extremely sensitive probes of departures from the standard cosmological model. In this work, we analyze the full BICEP1 three-year spectra [17] for evidence of polarization rotation, considering systematic uncertainties including our primary and alternate polarization calibrations, and exploring constraints on cosmological birefringence. We then use this polarization angle to self calibrate detector polarization orientations and calculate the tensor-to-scalar ratio from the self-calibrated BB spectrum.

The outline of the paper is as follows: Sec. II contains a review of polarization rotation and how it affects the observed CMB power spectra. The data sets and analysis procedure are described in Sec. III. Results and consistency checks are presented in Sec. IV. The impact of instrumental systematics is discussed in Sec. V. Consistency of the data with different birefringence models is in Sec. VI. Application of self calibration and its effect on the tensor-to-scalar ratio, r , are in Sec. VII, and we discuss our results in Sec. VIII.

TABLE I. Previous rotation angle constraints from CMB experiments, following [12]. Systematic uncertainties are shown in parentheses, where provided.

Experiment	Frequency (GHz)	ℓ range	α (degrees)
WMAP7 [13]	41 + 61 + 94	2–800	$-1.1 \pm 1.4(\pm 1.5)$
BOOM03 [14]	143	150–1000	-4.3 ± 4.1
QUaD [15]	100	200–2000	$-1.89 \pm 2.24(\pm 0.5)$
QUaD [15]	150	200–2000	$+0.83 \pm 0.94(\pm 0.5)$

II. POLARIZATION ROTATION OF THE CMB POWER SPECTRA

The CMB can be described by the statistical properties of its temperature and polarization. E - and B -mode polarization can be formed from linear combinations of the Stokes Q and U parameters. Maps of the temperature, T , and Stokes parameters, Q and U , are expanded in scalar and spin ± 2 spherical harmonics [18,19] to obtain

$$\begin{aligned} T(\hat{n}) &= \sum_{\ell,m} a_{\ell m}^T Y_{\ell m}(\hat{n}) \\ (Q \pm iU)(\hat{n}) &= \sum_{\ell,m} a_{\pm 2, \ell m \pm 2} Y_{\ell m}(\hat{n}), \end{aligned} \quad (1)$$

where the E - and B -modes of polarization have expansion coefficients $a_{\ell m}^E$ and $a_{\ell m}^B$ which can be expressed in terms of the spin ± 2 coefficients

$$a_{\pm 2, \ell m} = a_{\ell m}^E \pm i a_{\ell m}^B. \quad (2)$$

The spherical harmonic coefficients, $a_{\ell m}$, are characterized by their statistical properties,

$$\begin{aligned} \langle a_{\ell m}^X \rangle &= 0 \\ \langle a_{\ell m}^{X*} a_{\ell' m'}^{X'} \rangle &= C_{\ell}^{XX'} \delta_{\ell \ell'} \delta_{mm'}, \end{aligned} \quad (3)$$

where X and X' are either T , E or B . Here, $\langle a \rangle$ stands for the ensemble average. The polarization modes, E and B , are pure parity states (even and odd, respectively) and thus the correlation over the full sky of the B -mode with either the temperature or E -mode polarization vanishes [18,19]. However, if the polarization of the CMB is rotated, there will be a mixing between E and B , subsequently inducing TB and EB power spectra (Fig. 1):

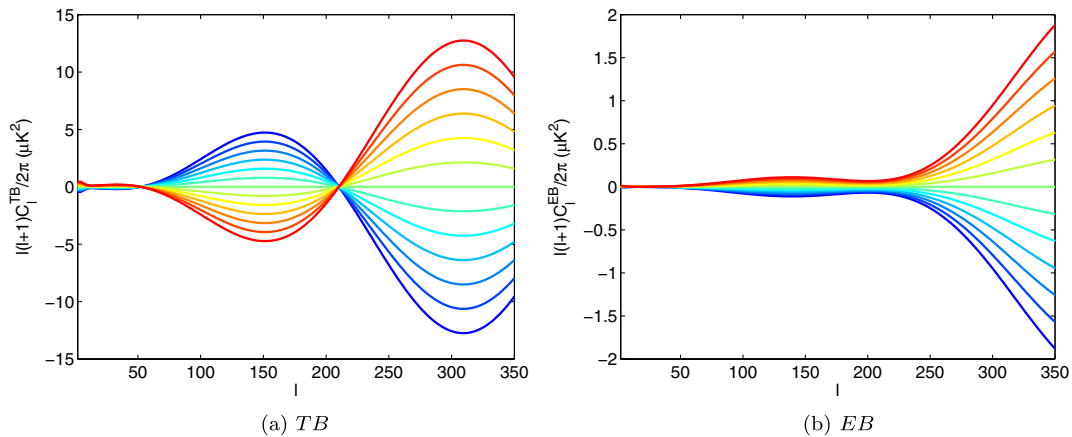


FIG. 1 (color online). Standard Λ CDM power spectra after applying polarization rotation of -3° (blue) to $+3^\circ$ (red), in 0.5° steps, for TB (left) and EB (right).

$$\begin{aligned} C_{\ell}^{TT} &= C_{\ell}^{TT} \\ C_{\ell}^{TE} &= C_{\ell}^{TE} \cos(2\alpha) \\ C_{\ell}^{EE} &= C_{\ell}^{EE} \cos^2(2\alpha) + C_{\ell}^{BB} \sin^2(2\alpha) \\ C_{\ell}^{BB} &= C_{\ell}^{EE} \sin^2(2\alpha) + C_{\ell}^{BB} \cos^2(2\alpha) \\ C_{\ell}^{TB} &= C_{\ell}^{TE} \sin(2\alpha) \\ C_{\ell}^{EB} &= \frac{1}{2} (C_{\ell}^{EE} - C_{\ell}^{BB}) \sin(4\alpha). \end{aligned} \quad (4)$$

No assumption has been made here as to the source of this rotation, namely whether or not it is cosmological. In the literature, α is identified with the birefringence rotation angle (see [13,15]), though here it is used to denote polarization rotation of any origin.

III. DATA AND ANALYSIS METHODOLOGY

BICEP1 observed for three years at the South Pole in three frequency bands: 100, 150 and 220 GHz, and released two-year results from 100 and 150 GHz frequency-combined spectra in [16] and three-year frequency-combined spectra in [17]. Results from the BICEP1 100, 150, and 220 GHz observations of the galactic plane are in [20] and from Faraday rotation modulators in [21].

We employ maximum-likelihood estimation for determining the best-fit polarization rotation angles of the power spectra following Eq. (4). We use two methods to construct the likelihoods, a Gaussian bandpower likelihood approximation and the Hamimeche-Lewis likelihood construction [22].

A. Data sets

We calculate rotation angles from the three-year frequency combined “all-spectra” estimator, where all-spectra is defined as $TE + EE + BB + TB + EB$. We can break this down by frequency and by spectral estimator for consistency checks. From this, we get four frequency

subsets consisting of the two frequency autospectra: 100 GHz autospectra (denoted “100”) and 150 GHz autospectra (denoted “150”), and the two frequency cross spectra: 100 GHz cross correlated with 150 GHz (denoted “cross”) and 150 GHz cross correlated with 100 GHz (denoted “alt-cross”). Note that although the EE and BB spectra are identical for the cross and alt-cross data sets, the TB and EB spectra are not, e.g., $T^{100}B^{150} \neq T^{150}B^{100}$. Plots of the TB and EB spectra for these four frequency subsets are in Fig. 2.

In addition, we have four spectral combinations to constrain α : the TB and EB modes as well as the combination of $TB + EB$, and all-spectra: $TE + EE + BB + TB + EB$ since polarization rotation also affects TE , EE , and BB ; however, from Eq. (4), we can see that for small α the rotated TE , EE , and BB deviate from the unrotated spectra by order α^2 and thus their constraining power for α is much weaker than the TB and EB spectra, which are linear in α . In addition, since they are quadratic in α , the sign of α cannot be directly determined. TB or EB break this sign degeneracy. These are not independent estimators but are useful as any unexpected discrepancies can be used to test the validity of the analysis.

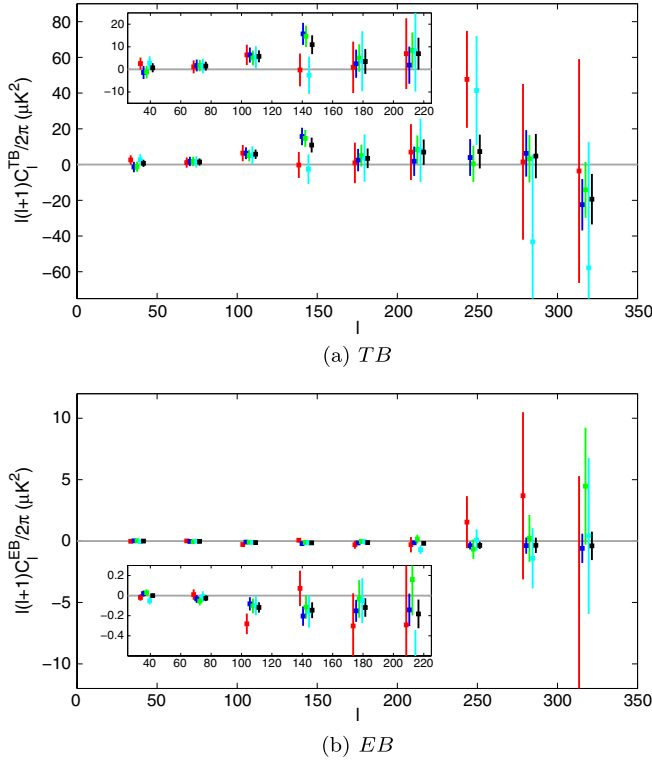


FIG. 2 (color online). BICEP1 TB and EB power spectra for all frequency combinations: 100 GHz autospectra (red), 150 GHz autospectra (blue), 100 \times 150 GHz cross-spectra (green), 150 \times 100 GHz “alt-cross” spectra (cyan), and frequency combined 100 + 150 GHz spectra (black). The points have been displaced in ℓ for clarity.

B. Likelihood analysis

We employ two likelihood constructions for this analysis: a Gaussian bandpower likelihood approximation and the more accurate Hamimeche-Lewis (HL) likelihood approximation [22]. The two likelihood constructions produce similar results, although we use the HL method for the final results since it more accurately treats cross-spectra covariances. We test both likelihood constructions for any biases and, in simulations, we find they accurately recover known input rotation angles.

For both methods, we calculate $\chi^2 = -2 \ln \mathcal{L}$, where χ^2 is defined in Eq. (6), below. We found the rotation angle that maximized the likelihood, and constructed 1σ error bars by finding the minimum-width 68% credible interval, assuming a uniform prior on α , for both likelihood constructions.

1. Gaussian bandpower likelihood approximation

This method was chosen due to its computational efficiency for isolating individual spectral estimators without including corresponding autospectra. Here, the difference between the observed spectra and theory spectra including rotation,

$$\Delta_b^{XY}(\alpha) = \hat{\mathcal{D}}_b^{XY} - \mathcal{D}_b^{XY}(\alpha), \quad (5)$$

is computed as a function of rotation angle, α , for each BICEP1 multipole bin, where BICEP1 reports nine bins of uniform width $\Delta\ell = 35$, with the first bin spanning $20 \leq \ell < 55$ and the ninth bin spanning $300 \leq \ell < 335$. Here, $\hat{\mathcal{D}}_b^{XY}$ is the measured BICEP1 XY power spectrum and $\mathcal{D}_b^{XY}(\alpha)$ is the theoretical rotated bandpower for XY for a given α . We use \mathcal{D}_b^{XY} to denote binned estimates of $\mathcal{D}_\ell^{XY} = \ell(\ell+1)C_\ell^{XY}/2\pi$. Here, $XY = TB$ or EB for each frequency combination. The χ^2 statistic is then constructed using

$$\chi_{XY}^2(\alpha) = \sum_{bb'} \Delta_b^{XY}(\alpha) \mathcal{M}_{bb'}^{-1} \Delta_{b'}^{XY}(\alpha), \quad (6)$$

where $\mathcal{M}_{bb'}$ is the covariance between multipole bins b and b' , as described in [17].

2. Hamimeche-Lewis method

The Hamimeche-Lewis method is the bandpower likelihood approximation used in [17]. As before, the χ^2 statistic is constructed as in Eq. (6) but following the procedure outlined in [17]. One crucial difference between this method and the Gaussian bandpower likelihood approximation is that XY includes all combinations of the spectra X and Y . For example, for EB , this method does not calculate the χ^2 for EB but actually the χ^2 which includes $EB + EE + BB$ —the comparison of the measured spectra to theoretical rotated spectra for EB , EE and BB .

simultaneously. To calculate the χ^2 statistic for any “pure” spectral combination using this method, we calculate the χ^2 of the full spectral combination and subtract off the other spectral combinations. For example, for EB , $\chi_{EB}^2 = \chi_{EE+BB+EB}^2 - \chi_{EE}^2 - \chi_{BB}^2$.

IV. ROTATION ANGLE RESULTS

The rotation angle, α , was calculated using the HL method from the standard BICEP1 three-year frequency combined spectra. The best-fit rotation angle is $\alpha = -2.77^\circ \pm 0.86^\circ$, where the quoted uncertainty is purely statistical. These spectra use our standard calibration of detector polarization angles from a dielectric sheet; systematic uncertainty on this calibration is discussed below in Sec. V. Figure 3 plots the peak-normalized HL likelihood and Fig. 4 shows the best-fit rotation angle spectra plotted compared to the BICEP1 three-year data and 499 simulated Λ CDM realizations (i.e., with $\alpha = 0$).

A. Consistency between analysis methods

To check that the rotation angle is not dependent on the analysis method, polarization rotation angles derived from the two analysis methods were compared. In Fig. 5, the likelihoods calculated for TB , EB and $TB + EB$ for the frequency-combined spectra for both the HL and Gaussian bandpower likelihood approximations are overplotted. For all three available spectral estimators, the analysis methods agree to within 0.32σ , 0.30σ and 0.18σ for TB , EB and $TB + EB$, respectively.

B. Consistency between frequencies

For consistency, the different frequency combinations were checked to determine if they have similar rotation angles. Table II shows the calculated rotation angles from

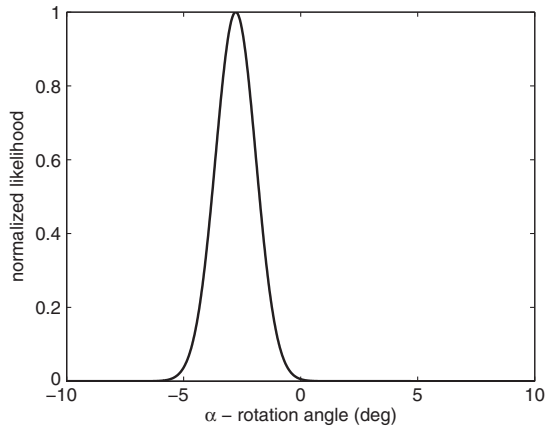


FIG. 3. The peak-normalized Hamimeche-Lewis likelihood for the all-spectra (“TEB”) rotation angle. The maximum likelihood value is -2.77° and the 68% confidence limits are $\pm 0.86^\circ$ from the peak value, corresponding to 3.22σ statistical significance.

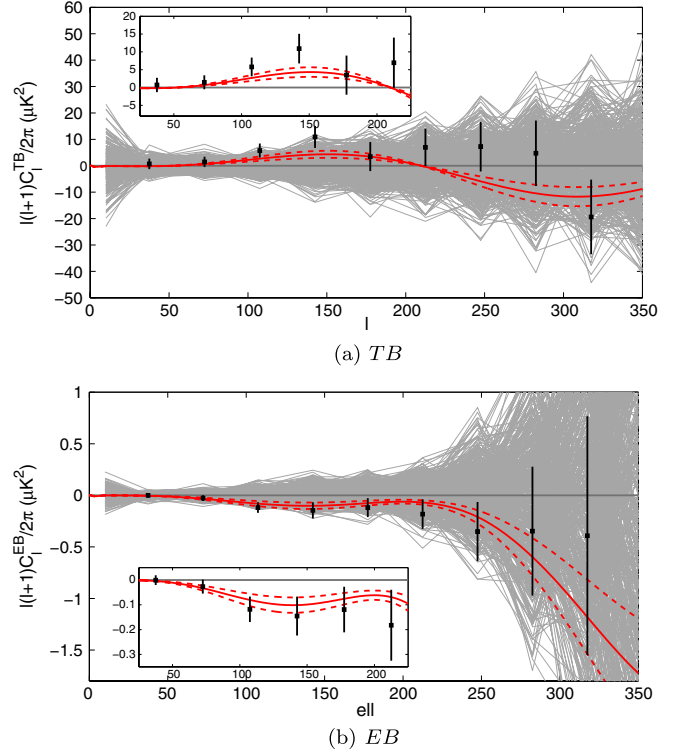


FIG. 4 (color online). Frequency-combined three-year BICEP1 spectra (black points) shown with the theoretical rotated spectra from the best-fit all-spectra rotation angle, $\alpha = -2.77^\circ \pm 0.86^\circ$ (red solid), the 1σ confidence limits (red dashed), and the 499 simulation realizations (gray). All simulation realizations assume $\alpha = 0$.

each frequency data set and for all four spectral estimators. Figure 6 shows the HL likelihoods for the all-spectra (TEB) rotation angles for each data set.

C. Consistency with Planck temperature taps

The TB spectrum estimate of the polarization rotation explicitly depends on the BICEP1 measurement of temperature. To check for systematics in the TB power spectrum, we replace BICEP1 maps with Planck temperature maps [23] for both 100 and 150 GHz and find the recovered angles agree to within 0.2σ .

V. IMPACT OF INSTRUMENTAL SYSTEMATIC EFFECTS

BICEP1 was the first experiment designed specifically to measure the B -mode power spectrum in order to constrain the inflationary cosmological model [24]. Accordingly, the analysis of instrumental systematics focused on potential bias of the BB spectrum and the tensor-to-scalar ratio with a benchmark of $r = 0.1$ [25]. Here, we extend the analysis to include the impact of measured systematics on the TB and EB power spectra for the three-year data set.

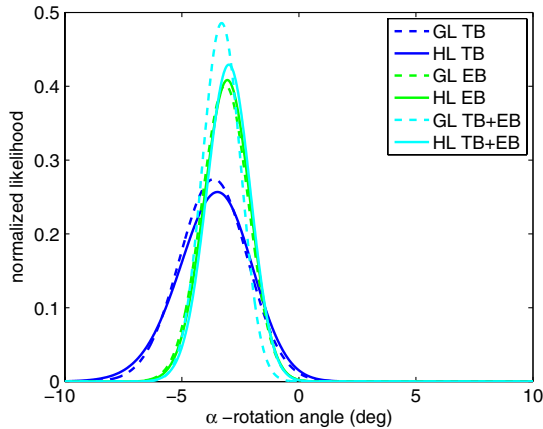


FIG. 5 (color online). Comparison of the two likelihood methods employed for the rotation angle calculation for the frequency-combined data. Likelihoods computed from the Gaussian bandpower likelihood approximation are shown as dashed lines and the Hamimeche-Lewis method likelihoods are shown as solid lines. The *TB* likelihood is in blue, *EB* is in green, and the *TB + EB* likelihood is cyan. The likelihoods have been normalized by their integral over α .

A. Polarization angle calibration

An error in the detector polarization angles used for map making is the only systematic which is completely degenerate with a rotation due to isotropic cosmic birefringence, and the only systematic capable of producing self-consistent *TB* and *EB* power spectra [26]. This calibration requirement is much more stringent when attempting to measure α than for r .

Calibrating detector angles for CMB polarimeters is very challenging. Some commonly employed methods include man-made calibrators, such as polarizing dielectric sheets [24,25] or polarization-selecting wire grids [27,28], and observations of polarized astronomical sources [29,30]. Man-made polarization calibration sources suffer from a host of challenges: they are often situated in the near field of the telescope, they can be unstable over long time scales, and they can be cumbersome to implement and align. Astronomical sources are not visible from all observatories and even the best characterized sources have orientations measured to an accuracy of only 0.5° [31]. In addition, the brightness of both astronomical and man-made calibration sources can overload the detectors, forcing them into a nonlinear response regime [32].

BICEP1 employed several hardware calibrators to measure detector polarization angles. The primary calibration comes from a dielectric sheet calibrator (DSC), described in detail in [25], but additional calibrations were made using sources with polarizing wire grids in the near and far field. The BICEP1 beam size and observatory location prevented polarization calibration using astronomical sources.

The polarization angle measurement from the DSC was performed the most frequently and is the best studied,

TABLE II. Maximum likelihood value and 1σ error for α . All numbers are in degrees.

Dataset	<i>TB</i> only	<i>EB</i> only	<i>TB + EB</i>	All-spectra
100 GHz	$-1.79^{+3.18}_{-3.14}$	$-3.53^{+2.38}_{-2.26}$	$-2.27^{+2.06}_{-1.98}$	$-2.27^{+2.06}_{-2.02}$
150 GHz	$-4.37^{+1.92}_{-1.78}$	$-2.95^{+1.20}_{-1.18}$	$-3.13^{+1.14}_{-1.12}$	$-2.91^{+1.06}_{-1.04}$
Cross	$-3.93^{+1.84}_{-1.74}$	$-2.55^{+1.68}_{-1.60}$	$-2.83^{+1.28}_{-1.24}$	$-2.67^{+1.20}_{-1.18}$
Alt-cross	$-2.71^{+3.52}_{-3.74}$	$-3.25^{+2.26}_{-2.20}$	$-3.45^{+2.24}_{-2.18}$	$-3.15^{+1.96}_{-2.00}$
Comb	$-3.47^{+1.66}_{-1.56}$	$-3.05^{+1.00}_{-0.96}$	$-2.99^{+0.94}_{-0.92}$	$-2.77^{+0.86}_{-0.86}$

which is why it was chosen for results in [16,17], as well as this work. Repeated measurements during each observing season produced polarization angles that agree with an root-mean-square (rms) error of 0.1° . However, measurements taken before and after focal plane servicing between the 2006 and 2007 observing seasons show an unexplained rotation of 1° in the polarization angles. There is also some uncertainty in translating the results of the DSC measurement to parameters appropriate for CMB analysis. The details of the polarized signal from the dielectric sheet depend on the near-field response of each detector, which is not well characterized.

We also consider two alternate calibrations for the detector polarization angles, which were both described in [25] as methods to measure the cross-polar response of the detectors. The first is a modulated broadband noise source, broadcasting via a rectangular feedhorn located behind a polarizing wire grid. The source is located on a mast at a range of 200 meters. We measure the detector response as a function of angle by scanning over the source with 18 different detector orientations. The advantage of this method is that the source is in the far field of the telescope. A challenge is that the observations require the use of a flat mirror, complicating the pointing model. In addition, it takes a significant amount of time to perform scans at all 18 orientations, which makes it more difficult to maintain stable source brightness. For BICEP2, we have invested significant effort in improving polarization orientation calibrations with the far-field broadband noise source, both by developing a high-precision rotating polarized source and improving the pointing model used for calibration analysis. These improvements were motivated by BICEP1 experience with systematic uncertainties on both the DSC and broadband source calibrations.

Another polarization angle calibrator consists of a wire grid covering a small aperture that is chopped between an ambient temperature absorber and cold sky. For calibrations, this source is installed in the near field of the telescope and the wire grid is rotated to measure detector polarization angles. The interpretation of results from this source has significant uncertainty because the small aperture probes only a small fraction of the detector near field response, yet the results are extrapolated to the full beam response.

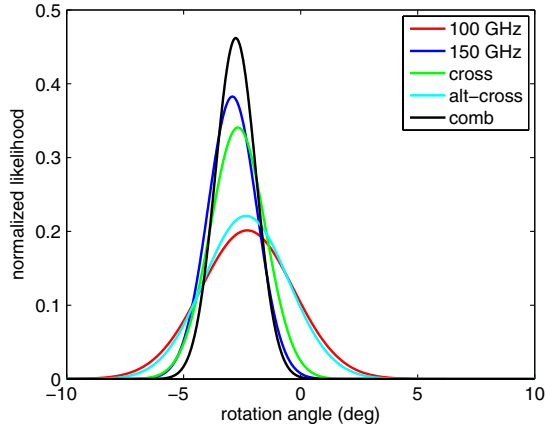


FIG. 6 (color online). Comparison of integral-normalized Hamimeche-Lewis method likelihoods of all-spectra (TEB) rotation angles for 100 GHz autospectra (red), 150 GHz autospectra (blue), 100×150 GHz cross spectra (green), 150×100 GHz “alt-cross” spectra (cyan), and frequency-combined spectra (black).

Table III lists the values of α measured from maps made using each of the polarization angle calibrations. Also shown is the result obtained if we simply assume that the detector polarization angles are as designed. These derived α values are qualitatively consistent with the average difference in the detector polarization angles between any two calibration methods, though the details depend on how each detector is weighted in the three-year maps. Besides the global rotations between each calibration method, which contribute to the variation in α , the per-detector polarization angles show scatter of $0.6\text{--}0.9^\circ$ between methods, much larger than the 0.1° consistency seen from repeated measurements using the DSC. Despite this scatter, we can observe significant structure in the pattern of polarization angles from detector to detector, which is not present in the as-designed angles.

From consideration of the 1.14° difference between α as derived from the DSC calibration and the mean of the three alternate calibrations, which have very different sources of systematic uncertainty, as well as the 1° shift observed in the DSC calibration results between observing seasons, we assign a calibration uncertainty of 1.3° on the overall orientation from the DSC calibration. We believe this upward revision of the 0.7° uncertainty quoted for this same calibration in [25] is warranted by the tension with the alternate calibrations. While this systematic error is larger than the 0.86° statistical error on α , we stress the fact that the polarization angle calibration is quite a bit better than what is needed to meet the $r = 0.1$ benchmark for the primary BICEP1 science goal.

In Sec. VII, we adopt a different approach and self-calibrate the polarization orientations by rotating the polarization maps to minimize α . Note that the calibration uncertainty on α applies only when we use the DSC

TABLE III. Polarization rotation angles derived using different detector polarization angle calibrations: the dielectric sheet calibrator (DSC), the far-field wire grid broadband noise source, the near-field wire grid aperture source, and assuming the polarization angles are as designed. For all cases, the statistical uncertainty on α is 0.86° .

Calibration method	Near/far field	α (degrees)
DSC	near	-2.77
Wire grid broadband source	far	-1.71
Wire grid aperture source	near	-1.91
As designed	—	-1.27

calibrated maps and attempt to measure astrophysical polarization rotation. To judge how well the self-calibration procedure can debias the B -mode map, only the statistical error is relevant.

B. Differential beam effects

Differential beam mismatches potentially mix E -modes and B -modes or leak intensity to either E - or B -mode polarization. Here, we investigate the impact of differential beam size, differential relative gain, differential pointing, and differential ellipticity on the derived rotation angle.

Beam systematics affect the EB spectra in a different way than TB spectra [33,34]. As a result, the scale dependence of the beam systematic polarization will imply a different *effective* rotation angle in the TB spectrum versus the EB spectrum, for a fixed ℓ -range.

The BICEP1 beams were measured in the lab prior to deployment using a source in the far field (50 meters from the aperture) and each observing season during summer calibration testing. Beam maps were fit to a two-dimensional elliptical Gaussian model which included a beam location, width, ellipticity, and orientation of the major axis of the ellipse with respect to the polarization axes.

1. Differential beam size

Though the differential beam size effect can leak temperature to polarization, due to circular symmetry it will not break the parity of the underlying sky and thus cannot generate the parity-odd TB and EB modes [33].

2. Differential relative gain

As with differential beam size, circular symmetry is preserved by differential relative gain and thus there is no breaking of the parity of the sky which would generate TB and EB modes [33]. We ran differential gain simulations using observed values and random values drawn from a Gaussian distribution with an rms of 1%. None of the simulations showed polarization rotation greater in magnitude than 0.25° .

A significant difference between the BICEP1 two-year results reported in [16] and the BICEP1 three-year power

spectra is that the three-year spectra undergo relative gain deprojection which reduces B -mode contamination due to this systematic to negligible levels [17].

3. Differential pointing

The effect of differential pointing is analytically calculated using the measured magnitude and direction of beam offsets with the expected amount of false BB power scaling as the square of the magnitude of the differential pointing, following the construction in [33]. The upper limit on differential pointing error was estimated to be $<1.3\%$ of the beam size. While this was found to be the dominant beam systematic effect for the BICEP1 limit on r [17], it is clear from Fig. 7 that differential pointing does not induce TB or EB , and has a negligible effect on the polarization rotation angle estimation. This was calculated for the worst-case scanning strategy and therefore provides very conservative bounds on the TB and EB produced.

4. Differential ellipticity

Differential ellipticity values were derived by fitting each measured beam in a detector pair for ellipticity and then differencing those values for the two detectors in a pair. The fits were generally not repeatable when the telescope was rotated about its boresight angle, so only upper limits on differential ellipticity are quoted. The BICEP1 estimated differential ellipticity is $<0.2\%$.

As with differential pointing, we calculate the TB and EB following the construction in [33]. As before, this is for the worst-case scenario, where the major axes of the ellipticities are separated by 45° . From Fig. 7, it is clear that differential ellipticity can generate TB power which has a different spectral shape than that produced by

polarization rotation. In addition, the TB spectrum is inconsistent with the polarization rotation of EB .

C. Experimental consistency checks

To probe the susceptibility of BICEP1 data to systematic effects irrespective of origin, [16] created six null tests or “jackknife” spectra that were used as consistency tests. These tests involve splitting the data in two halves and differencing them. The two halves are chosen to illuminate systematics since signals which are common to both data sets will cancel, and the resultant jackknife will either be consistent with noise or indicate contamination. The jackknife splits are by boresight rotation, scan direction, observing time, detector alignment, elevation coverage, and frequency, as described in [16,17].

In the power spectrum analyses [16,17], the jackknife maps were obtained by differencing the maps for each half whereas here we ran each jackknife half through the full analysis pipeline to produce power spectra. Unlike in the previous analyses, we did not look for consistency with zero but self consistency between jackknife halves. We fit rotation angles for each jackknife half and difference the resultant best-fit angles to form $\Delta\alpha$. Only the frequency-combined spectra are used to improve the constraining power of these tests. We then calculate the probability to exceed (PTE) the observed $\Delta\alpha$ value by chance, given measurement uncertainties. These results are shown in Fig. 8. If there is an instrumental systematic contribution to a detection of α that is tested using these null tests, then excess PTE values near zero will arise. The jackknife halves are considered consistent if they meet the following three criteria: (1) fewer than 5% of the jackknives have PTE values smaller than 5%, (2) none of the PTE values are excessively small (defined as $\ll 1\%$), and (3) the PTE value from all jackknives are consistent with a uniform

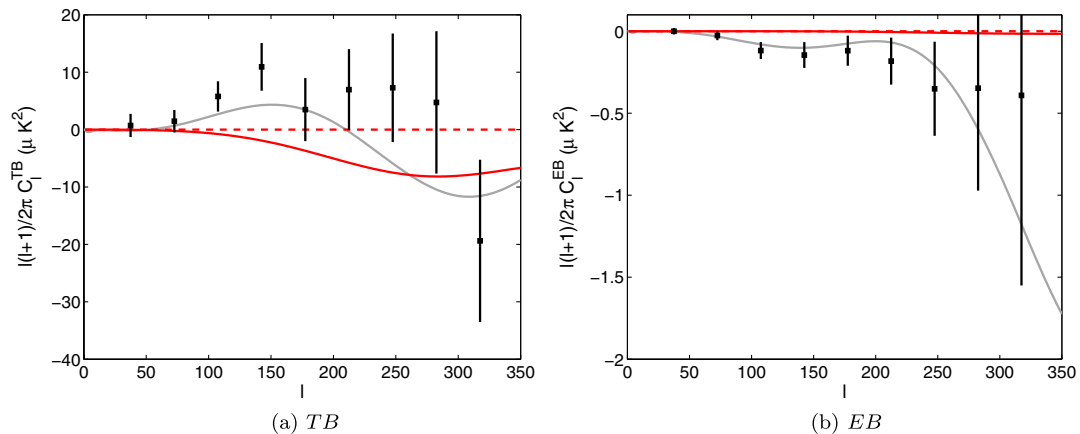


FIG. 7 (color online). A plot of the effects of differential ellipticity (red solid line) and differential pointing (red dashed line) on the TB (left) and EB (right) power spectra. The gray line shows the power spectra with $\alpha = -2.77^\circ$. The black points are the frequency-combined three-year band powers. The differential ellipticity and differential pointing are at the level of 0.2% and 1.3%, respectively, corresponding to the upper limits reported in [25]. In both cases, the systematic curves correspond to “worst-case” scenarios: the major axes of the ellipticities are separated by 45° and differential pointing assumes a poorly chosen scan strategy [34].

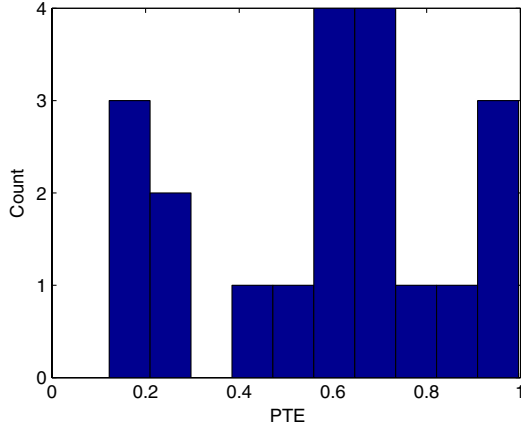


FIG. 8 (color online). A histogram of the probability to exceed values for the measurement of $\Delta\alpha$ in each of the jackknife spectra. There are 20 spectral combinations (which are not all independent): TB , EB , $TB + EB$, and all-spectra estimators for the frequency-combined spectra for each of the five jackknife tests.

distribution between zero and one. Given the consistency of the jackknife PTEs with these criteria, systematics probed by these jackknives are not the source of the observed polarization rotation angle.

VI. CONSTRAINTS ON FREQUENCY-DEPENDENT COSMOLOGICAL BIREFRINGENCE

This paper has focused on the assumption that polarization rotation is independent of electromagnetic frequency. However, several models feature polarization rotation that predicts a manifestly frequency-dependent rotation angle. One such birefringence model has been proposed by Contaldi, Dowker, and Philpott in [35], hereafter called the “CDP” model.

Another effect which could cause frequency-dependent polarization rotation would be Faraday rotation of CMB polarization due to the Milky Way’s magnetic field.

A. Contaldi-Dowker-Philpott model

In the CDP model, there are two electromagnetic frequency-dependent parameters (μ and χ) leading to the following power spectra:

$$\begin{aligned}
 C_{\ell}^{TT} &= C_{\ell}^{TT} \\
 C_{\ell}^{TB} &= e^{-\mu} C_{\ell}^{TE} \sin(2\chi) \\
 C_{\ell}^{EB} &= \frac{1}{2} e^{-2\mu} (C_{\ell}^{EE} - C_{\ell}^{BB}) \sin(4\chi) \\
 C_{\ell}^{TE} &= e^{-\mu} C_{\ell}^{TE} \cos(2\chi) \\
 C_{\ell}^{EE} &= e^{-2\mu} C_{\ell}^{EE} \cos^2(2\chi) + e^{-2\mu} C_{\ell}^{BB} \sin^2(2\chi) \\
 C_{\ell}^{BB} &= e^{-2\mu} C_{\ell}^{EE} \sin^2(2\chi) + e^{-2\mu} C_{\ell}^{BB} \cos^2(2\chi), \quad (7)
 \end{aligned}$$

TABLE IV. Maximum likelihood values for the damping parameter, μ , and the rotation angle, χ , along with their 1σ error bars for the CDP model.

Frequency (GHz)	μ	χ (degrees)
100	$-0.017^{+0.073}_{-0.076}$	$-2.25^{+2.02}_{-2.02}$
150	$-0.029^{+0.042}_{-0.043}$	$-2.91^{+1.02}_{-1.02}$

where $\mu/\chi \sim 1/\nu$, and ν is the electromagnetic frequency (i.e., 100 and 150 GHz). Here, χ is a frequency-dependent rotation angle, and μ characterizes the frequency-dependent damping parameter. The frequency-independent spectra are obtained in the limit $\mu \rightarrow 0$, with χ identified with α .

As is evident from Eq. (7), to constrain the frequency-dependent CDP model, the TE , EE and BB spectra must also be included in the analysis in order to break the degeneracy between χ and μ .

The results for the damping parameter and rotation angle χ are presented in Table IV and Fig. 9. The inferred μ is consistent with zero and μ/χ is not inversely proportional to ν , thus there is no compelling evidence for frequency dependent birefringence in the CDP picture.

B. Faraday rotation of galactic magnetic field

Faraday rotation due to the Milky Way’s magnetic field could produce frequency-dependent polarization rotation proportional to the inverse of the frequency squared [36]. Scaling the 150 GHz all-spectra estimator α by $(100/150)^{-2}$, we would expect to see polarization rotation of the 100 GHz spectra consistent with an $\alpha = -6.55^{+2.34}_{-2.39}$ degrees, whereas our 100 GHz all-spectra estimator results in a polarization rotation of $\alpha = -2.27^{+2.06}_{-2.02}$, corresponding to a 1.37σ discrepancy. While there is some tension between the predicted α and the measured α , Faraday rotation cannot be ruled out as the cause of the rotation.

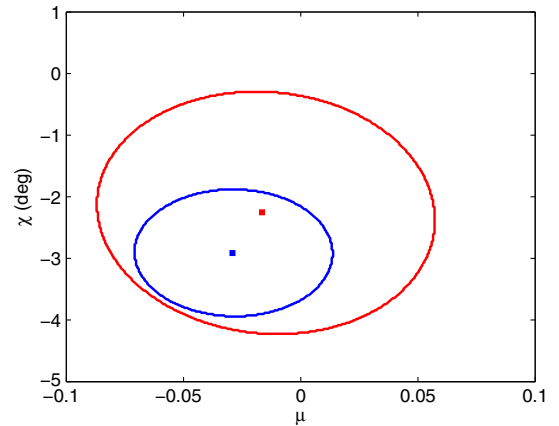


FIG. 9 (color online). Best-fit μ and χ values for the CDP model for 100 GHz (red point) and 150 GHz (blue point) from the all-spectra estimator, along with their 68% confidence interval contours (red and blue contours, respectively).

VII. SELF-CALIBRATED UPPER LIMIT ON TENSOR-TO-SCALAR RATIO

If the polarization rotation is systematic in nature, the derived rotation angle can be used to calibrate the detector polarization orientations [32]. The three-year all-spectra rotation angles were added to the polarization orientations treating the frequency bands as independent, i.e., only the 100 GHz (150 GHz) derived rotation angle was added to the 100 GHz (150 GHz) detectors. These self-calibrated polarization orientation angles were propagated through the power spectrum analysis pipeline [17]. The self-calibrated power spectra were analyzed for residual polarization rotation which yielded a rotation angle $\alpha = +0.01^\circ \pm 0.86^\circ$ from the frequency-combined all-spectra estimator, consistent with zero, as expected.

Any polarization rotation, regardless of cosmic or systematic origin, will positively bias r since E -mode power will be leaked into the B -mode spectrum [Eq. (4)]. There is also a reduction to the B -mode power spectrum due to B -modes leaking to E -modes; however, since the E -modes are significantly larger than the B -modes, the net result is a positive bias on the B -mode power spectrum. From the self-calibrated three-year power spectra, following the procedure in [17], we find the upper limit on the tensor-to-scalar ratio reduces from $r < 0.70$ to $r < 0.65$ at 95% confidence. From simulations, we find that the bias on r from self calibration with no underlying polarization rotation is less than 0.01.

VIII. CONCLUSION

The BICEP1 three-year data, when analyzed using detector polarization orientations from our standard dielectric sheet calibrator, show nonvanishing TB and EB spectra consistent with an overall polarization rotation of $-2.77^\circ \pm 0.86^\circ$ at 3.22σ significance. The significance for nonzero rotation of astrophysical origin is only 1.78σ , given the 1.3° systematic uncertainty on our orientation calibration which adds in quadrature. This result passes experimental consistency tests which probe for systematic differences of polarization rotation in various subsets of data. We rule out beam systematics as significant, and identify polarization orientation miscalibration as the primary concern among instrumental systematics. Isotropic cosmic birefringence cannot be excluded, though it is degenerate with a polarization miscalibration. The data show no compelling evidence for frequency-dependent isotropic cosmic birefringence models. An alternate use of the measurements described here is to self calibrate the detector polarization orientations, at the expense of losing constraining power on isotropic cosmological birefringence [32]. Self calibrating the BICEP1 three-year data reduces the upper limit on the tensor-to-scalar ratio from $r < 0.70$ to $r < 0.65$ at 95% confidence.

Future CMB polarimeters with improved polarization calibration methods will be needed to break the degeneracy between polarization rotation and detector polarization orientation uncertainty. In addition to the CMB, complementary astronomical probes such as the polarization orientation of radio galaxies and quasars [37,38] can help constrain cosmological birefringence. However, these objects can only constrain cosmic birefringence over a limited range of redshifts and only along particular lines of sight, whereas CMB polarization can be used to constrain cosmic birefringence over the entire sky and is sensitive to effects accrued over the history of the entire Universe. Polarization angles calibrated with current man-made or astronomical sources are accurate enough for current generation B -mode measurements, but are insufficiently characterized for cosmic birefringence searches. Based on BICEP1 experiences with systematic uncertainties on polarization orientation calibration reported in this paper, improved far-field calibrators have been developed for BICEP2 and other future experiments. The revolutionary discovery potential of a detection of cosmic birefringence motivates the development of more accurate hardware calibrators and further investigation of astronomical sources to achieve a precision of $\ll 0.5^\circ$. Ultimately, a combination of precisely understood man-made and astronomical sources will allow for powerful constraints on parity violation which will come concomitantly with bounds on the physics of inflation.

ACKNOWLEDGMENTS

BICEP1 was supported by NSF Grant No. OPP-0230438, Caltech Presidents Discovery Fund, Caltech Presidents Fund PF-471, JPL Research and Technology Development Fund, and the late J. Robinson. This analysis was supported in part by NSF CAREER Award No. AST-1255358 and the Harvard College Observatory, and J. M. K. acknowledges support from an Alfred P. Sloan Research Fellowship. B. G. K. acknowledges support from NSF PECASE Award No. AST-0548262. N. J. M.'s research was supported by an appointment to the NASA Postdoctoral Program at Goddard Space Flight Center, administered by Oak Ridge Associated Universities through a contract with NASA. M. S. acknowledges support from a grant from Joan and Irwin Jacobs. We thank the South Pole Station staff for helping make our observing seasons a success. We also thank our colleagues in the ACBAR, BOOMERANG, QUAD, BOLOCAM, SPT, WMAP and Planck experiments, as well as Kim Griest, Amit Yadav, and Casey Conger for advice and helpful discussions, and Kathy Deniston and Irene Coyle for logistical and administrative support. We thank Patrick Shopbell for computational support at Caltech and the FAS Science Division Research Computing Group at Harvard University for providing support to run all the computations for this paper on the Odyssey cluster.

- [1] S. M. Carroll, G. B. Field, and R. Jackiw, *Phys. Rev. D* **41**, 1231 (1990).
- [2] S. M. Carroll and G. B. Field, *Phys. Rev. Lett.* **79**, 2394 (1997).
- [3] S. M. Carroll, *Phys. Rev. Lett.* **81**, 3067 (1998).
- [4] A. Lue, L. Wang, and M. Kamionkowski, *Phys. Rev. Lett.* **83**, 1506 (1999).
- [5] S. Alexander and J. Martin, *Phys. Rev. D* **71**, 063526 (2005).
- [6] S. H. Alexander, M. E. Peskin, and M. M. Sheikh-Jabbari, *Phys. Rev. Lett.* **96**, 081301 (2006).
- [7] A. P. S. Yadav, R. Biswas, M. Su, and M. Zaldarriaga, *Phys. Rev. D* **79**, 123009 (2009).
- [8] V. Gluscevic, M. Kamionkowski, and A. Cooray, *Phys. Rev. D* **80**, 023510 (2009).
- [9] V. Gluscevic and M. Kamionkowski, *Phys. Rev. D* **81**, 123529 (2010).
- [10] J.-Q. Xia, H. Li, and X. Zhang, *Phys. Lett. B* **687**, 129 (2010).
- [11] J.-Q. Xia, *J. Cosmol. Astropart. Phys.* **1** (2012) 046.
- [12] G. Gubitosi and F. Paci, *J. Cosmol. Astropart. Phys.* **02** (2013) 020.
- [13] E. Komatsu *et al.*, *Astrophys. J. Suppl. Ser.* **192**, 18 (2011).
- [14] L. Pagano, P. de Bernardis, G. de Troia, G. Gubitosi, S. Masi, A. Melchiorri, P. Natoli, F. Piacentini, and G. Polenta, *Phys. Rev. D* **80**, 043522 (2009).
- [15] E. Y. S. Wu *et al.*, *Phys. Rev. Lett.* **102**, 161302 (2009).
- [16] H. C. Chiang *et al.*, *Astrophys. J.* **711**, 1123 (2010).
- [17] D. Barkats *et al.*, [arXiv:1310.1422](https://arxiv.org/abs/1310.1422).
- [18] U. Seljak, *Astrophys. J.* **482**, 6 (1997).
- [19] M. Kamionkowski, A. Kosowsky, and A. Stebbins, *Phys. Rev. D* **55**, 7368 (1997).
- [20] E. M. Bierman *et al.*, *Astrophys. J.* **741**, 81 (2011).
- [21] S. Moyerman *et al.*, *Astrophys. J.* **765**, 64 (2013).
- [22] S. Hamimeche and A. Lewis, *Phys. Rev. D* **77**, 103013 (2008).
- [23] P. A. R. Ade, N. Aghanim, C. Armitage-Caplan, M. Arnaud, M. Ashdown, F. Atrio-Barandela, J. Aumont, C. Baccigalupi, A. J. Banday *et al.* (Planck Collaboration), [arXiv:1303.5062](https://arxiv.org/abs/1303.5062) (unpublished).
- [24] B. G. Keating, P. A. Ade, J. J. Bock, E. Hivon, W. L. Hozapfel, A. E. Lange, H. Nguyen, and K. W. Yoon, *SPIE Proceedings* Vol. **4843** (SPIE-International Society for Optical Engineering, Bellingham, WA, 2003).
- [25] Y. D. Takahashi *et al.*, *Astrophys. J.* **711**, 1141 (2010).
- [26] A. P. S. Yadav, M. Shimon, and B. G. Keating, *Phys. Rev. D* **86**, 083002 (2012).
- [27] O. Tajima, H. Nguyen, C. Bischoff, A. Brizius, I. Buder, and A. Kusaka, *J. Low Temp. Phys.* **167**, 936 (2012).
- [28] E. M. George *et al.*, *SPIE Proceedings* Vol. **8452** (SPIE-International Society for Optical Engineering, Bellingham, WA, 2012).
- [29] P. C. Farese, G. Dall'Oglio, J. O. Gundersen, B. G. Keating, S. Klawikowski, L. Knox, A. Levy, P. M. Lubin, C. W. O'Dell, A. Peel, L. Piccirillo, J. Ruhl, and P. T. Timbie, *Astrophys. J.* **610**, 625 (2004).
- [30] C. Bischoff *et al.*, *Astrophys. J.* **768**, 9 (2013).
- [31] J. Aumont, L. Conversi, C. Thum, H. Wiesemeyer, E. Falgarone, J. F. Macias-Perez, F. Piacentini, E. Pointecouteau, N. Ponthieu, J. L. Puget, C. Rosset, J. A. Tauber, and M. Tristram, [arXiv:0912.1751](https://arxiv.org/abs/0912.1751) [*Astron. Astrophys.* (to be published)].
- [32] B. G. Keating, M. Shimon, and A. P. S. Yadav, *Astrophys. J.* **762**, L23 (2013).
- [33] M. Shimon, B. Keating, N. Ponthieu, and E. Hivon, *Phys. Rev. D* **77**, 083003 (2008).
- [34] N. J. Miller, M. Shimon, and B. G. Keating, *Phys. Rev. D* **79**, 103002 (2009).
- [35] C. R. Contaldi, F. Dowker, and L. Philpott, *Classical Quantum Gravity* **27**, 172001 (2010).
- [36] S. De, L. Pogosian, and T. Vachaspati, *Phys. Rev. D* **88**, 063527 (2013).
- [37] S. di Serego Alighieri, [arXiv:1011.4865](https://arxiv.org/abs/1011.4865).
- [38] M. Kamionkowski, *Phys. Rev. D* **82**, 047302 (2010).